



HAL
open science

Small-wedge synchrotron and serial XFEL datasets for Cysteinyl leukotriene GPCRs

Egor Marin, Aleksandra Luginina, Anastasiia Gusach, Kirill Kovalev, Sergey Bukhdruker, Polina Khorn, Vitaly Polovinkin, Elizaveta Lyapina, Andrey Rogachev, Valentin Gordeliy, et al.

► **To cite this version:**

Egor Marin, Aleksandra Luginina, Anastasiia Gusach, Kirill Kovalev, Sergey Bukhdruker, et al.. Small-wedge synchrotron and serial XFEL datasets for Cysteinyl leukotriene GPCRs. *Scientific Data*, 2020, 7 (1), pp.388-1-388-13. 10.1038/s41597-020-00729-2 . hal-03725765

HAL Id: hal-03725765

<https://hal.science/hal-03725765>

Submitted on 18 Jul 2022

HAL is a multi-disciplinary open access archive for the deposit and dissemination of scientific research documents, whether they are published or not. The documents may come from teaching and research institutions in France or abroad, or from public or private research centers.

L'archive ouverte pluridisciplinaire **HAL**, est destinée au dépôt et à la diffusion de documents scientifiques de niveau recherche, publiés ou non, émanant des établissements d'enseignement et de recherche français ou étrangers, des laboratoires publics ou privés.



OPEN

DATA DESCRIPTOR

Small-wedge synchrotron and serial XFEL datasets for Cysteinyll leukotriene GPCRs

Egor Marin¹, Aleksandra Luginina¹, Anastasiia Gusach^{1,10}, Kirill Kovalev^{1,2,3,4,7}, Sergey Bukhdruker^{1,3,7,11}, Polina Khorn¹, Vitaly Polovinkin^{2,3,9}, Elizaveta Lyapina¹, Andrey Rogachev^{1,8}, Valentin Gordeliy^{1,2,3,4,7}, Alexey Mishin¹, Vadim Cherezov^{1,5,6} & Valentin Borshchevskiy^{1,3,7}✉

Structural studies of challenging targets such as G protein-coupled receptors (GPCRs) have accelerated during the last several years due to the development of new approaches, including small-wedge and serial crystallography. Here, we describe the deposition of seven datasets consisting of X-ray diffraction images acquired from lipidic cubic phase (LCP) grown microcrystals of two human GPCRs, Cysteinyll leukotriene receptors 1 and 2 (CysLT₁R and CysLT₂R), in complex with various antagonists. Five datasets were collected using small-wedge synchrotron crystallography (SWSX) at the European Synchrotron Radiation Facility with multiple crystals under cryo-conditions. Two datasets were collected using X-ray free electron laser (XFEL) serial femtosecond crystallography (SFX) at the Linac Coherent Light Source, with microcrystals delivered at room temperature into the beam within LCP matrix by a viscous media microextrusion injector. All seven datasets have been deposited in the open-access databases Zenodo and CXIDB. Here, we describe sample preparation and annotate crystallization conditions for each partial and full datasets. We also document full processing pipelines and provide wrapper scripts for SWSX and SFX data processing.

Background & Summary

Cysteinyll leukotrienes, produced from arachidonic acid via the 5-lipoxygenase pathway, are pro-inflammatory mediators that modulate vascular permeability and immune response; hence, they are involved in multiple disorders including asthma, cardiovascular diseases and cancer¹. Cysteinyll leukotrienes elicit their action through two G protein-coupled receptors (GPCRs), CysLT₁R and CysLT₂R, that share 38% sequence identity¹. CysLT₁R is mostly expressed in the lungs and immune cells, and its stimulation leads to allergic symptoms in the airways². CysLT₂R is found additionally in cardiovascular and brain tissues, with demonstrated involvement in ischemia and acute brain injuries^{3,4}, however, the role of this receptor remains controversial and poorly understood. Both CysLT₁R and CysLT₂R have been implicated in progression of various cancers^{5–8}, while the mutated form of CysLT₂R with L129Q substitution has been associated with uveal melanoma^{9,10}. Thus, CysLTRs are important pharmaceutical targets¹¹, what inspired us to determine their high-resolution structures in complex with antiasthmatic drugs and other prospective antagonists.

¹Research Center for Molecular Mechanisms of Aging and Age-related Diseases, Moscow Institute of Physics and Technology, Dolgoprudny, 141701, Russia. ²Institut de Biologie Structurale (IBS), Université Grenoble Alpes, CEA, CNRS, Grenoble, France. ³Institute of Biological Information Processing (IBI-7: Structural Biochemistry), Forschungszentrum Jülich GmbH, 52425, Jülich, Germany. ⁴Institute of Crystallography, University of Aachen (RWTH), Aachen, Germany. ⁵Bridge Institute, Michelson Center for Convergent Bioscience, University of Southern California, Los Angeles, CA, 90089, USA. ⁶Department of Chemistry, University of Southern California, Los Angeles, CA, 90089, USA. ⁷JuStruct: Jülich Center for Structural Biology, Forschungszentrum Jülich GmbH, 52425, Jülich, Germany. ⁸Joint Institute for Nuclear Research, Dubna, 141980, Russia. ⁹ELI Beamlines, Institute of Physics, Czech Academy of Science, Na Slovance 2, 18221, Prague, Czech Republic. ¹⁰Present address: MRC Laboratory of Molecular Biology, Cambridge CB2 0QH, UK. ¹¹ESRF—The European Synchrotron, 38000, Grenoble, France. ✉e-mail: cherezov@usc.edu; borshchevskiy.vi@phystech.edu

Over the last few years, small-wedge synchrotron crystallography (SWSX) and serial femtosecond crystallography (SFX) have developed into powerful techniques, enabling high-resolution structure determination of many difficult to crystallize targets^{12,13}. Several approaches to data processing have been developed for both SFX¹³ and SWSX^{14–20}, and several papers reported deposition of raw serial crystallography data for challenging targets^{21–25}. Many datasets can be found online on SBGrid (data.scripps.edu), Zenodo (zenodo.org) or CXIDB (cxidb.org)²⁷; the latter is used for SFX and other XFEL-related data deposition, whereas SBGrid and Zenodo host SWSX among other types of data.

Recently, we have determined crystal structures of CysLT₁R²⁸ (PDB codes 6RZ4, 6RZ5) and CysLT₂R²⁹ (PDB codes 6RZ6, 6RZ7, 6RZ8, 6RZ9). Here, we present fully-annotated SWSX and SFX datasets for these structures, as well as unpublished SFX data of a new crystal form of CysLT₁R. The raw diffraction data, consisting of five SWSX and two SFX datasets, represent a wide range of resolutions (2.4–3.5 Å), SWSX miniset³⁰ wedge sizes (3–180°), and space groups (6 different space groups). We carefully document crystallization conditions and harvesting details for each dataset, allowing one to investigate crystal non-isomorphism. Finally, we describe all data processing steps, provide supporting code and intermediate results, aiming for reproducibility of deposited data processing.

Methods

The preparation of CysLT₁R and CysLT₂R samples, data collection, and processing have been described previously^{28,29}. Here, we provide a summary for each sample.

Construct engineering, expression, purification, and crystallization of CysLT₁R and CysLT₂R.

The human CysLT₁R gene (UniProt ID Q9Y271) was codon-optimized for expression in *Spodoptera frugiperda* (*Sf9*) insect cell line and modified for crystallization by a C-terminal truncation at K311 and by the insertion of a fusion protein BRIL³¹ (thermostabilized apocytochrome b₅₆₂ from *Escherichia coli* with mutations M7W, H102I, and R106L) in the third intracellular loop (ICL3) between K222 and K223 using the S and SG linkers on each side, respectively (Fig. 1a). For CysLT₂R, the human WT gene (UniProt ID Q9NS75) was modified by truncating amino acids 1–16 from the N-terminus and 323–346 from the C-terminus and inserting BRIL into ICL3 between residues E232 and V240. Three point mutations, W51^{1.45V}, D84^{2.50N}, and F137^{3.51Y} (superscripts refer to the receptor Ballesteros-Weinstein numbering of residues in Class A GPCR³²), were further introduced to improve receptor surface expression as well as its stability and yield (Fig. 1b).

Each gene of interest was cloned into a modified *pFastBac1* plasmid, containing a cleavable influenza hemagglutinin signal sequence (HA), a Flag tag, a AKLQTM linker, a 10 × His tag, and a Tobacco Etch Virus (TEV) protease site followed by KpnI restriction site on the N-terminal side of the inserted gene (Fig. 1c). The plasmid was then transfected into *Sf9* insect cells using the bac-to-bac expression system (Invitrogen). High-titer recombinant baculovirus (>3 × 10⁸ viral particles per ml) was obtained and used to infect *Sf9* cells at a density of (2–3) × 10⁶ cells per ml culture and a multiplicity of infection of 5–10 in the presence of a ligand: 8 μM zafirlukast (Cayman Chemical) for CysLT₁R or 3 μM BayCysLT₂ (Cayman Chemical) for CysLT₂R. The protein surface expression and the virus titer were measured using flow cytometry. Cells were harvested 48–50 hours post infection by centrifugation at 2,000 × g and stored at –80 °C until use.

Protein purification was conducted at 4 °C. For each protein-ligand complex, the relevant ligand was added during purification. Cells were thawed and lysed by repetitive homogenization with a glass douncer followed by ultracentrifugation (30 min at 220,000 × g), 2 times in hypotonic buffer (10 mM HEPES pH 7.5, 20 mM KCl, and 10 mM MgCl₂) and 3 times in high osmotic buffer (10 mM HEPES pH 7.5, 20 mM KCl, 10 mM MgCl₂, and 1 M NaCl) with the addition of a protease inhibitor cocktail (500 μM 4-(2-aminoethyl)benzenesulfonyl fluoride hydrochloride (Gold Biotechnology), 1 μM E-64 (Cayman Chemical), 1 μM Leupeptin (Cayman Chemical), 150 nM Aprotinin (A.G. Scientific)).

Membranes were then incubated for 30 min in 10 mM HEPES pH 7.5, 20 mM KCl, 10 mM MgCl₂, 2 mg ml⁻¹ iodacetamide, protease inhibitor cocktail, and 25 μM ligand. Then receptors were solubilized by the addition of an equal volume of solubilisation buffer (300 mM NaCl, 2% (w/v) n-dodecyl-β-D-maltopyranoside (DDM; Avanti Polar Lipids) 0.4% (w/v) cholesteryl hemisuccinate (CHS; Sigma), 10% glycerol) and incubation for 3.5 hours. After 1-hour centrifugation (650,000 × g) to remove insolubilized material, the supernatant was incubated with a TALON IMAC resin (Clontech) overnight in the presence of 10/20 mM imidazole, 100 mM HEPES pH 7.5 for CysLT_{1/2}R with NaCl concentration increased to 800 mM.

The resin was then washed with 10 column volumes (CV) of wash buffer I (8 mM ATP, 100 mM HEPES pH 7.5, 10 mM MgCl₂, 500 mM NaCl, 15 mM imidazole, 10 μM ligand, 10% glycerol, 0.1% DDM, 0.02% CHS), then with 5 CV of wash buffer II (25 mM HEPES pH 7.5, 250/500 mM NaCl for CysLT_{1/2}R, 30 mM imidazole, 10 μM ligand, 10% glycerol, 0.015% DDM, 0.003% CHS), then buffer was exchanged into buffer III (25 mM HEPES pH 7.5, 250/500 mM NaCl for CysLT_{1/2}R, 10 mM imidazole, 10 μM ligand, 10% glycerol, 0.05% DDM, 0.01% CHS) and the protein-containing resin was treated with PNGase F (Sigma) for 5 hours. Resin was further washed with 5 CV of wash buffer III and eluted with (25 mM HEPES pH 7.5, 250/500 mM NaCl for CysLT_{1/2}R, 300 mM imidazole, 10 μM ligand, 10% glycerol, 0.05% DDM, 0.01% CHS) in several fractions. After removing imidazole using a PD10 desalting column (GE Healthcare), the protein was incubated with 50 μM ligand and a His-tagged home-made TEV protease overnight to remove the N-terminal tags. Reverse IMAC was performed on the following day and the protein was concentrated up to 50–70 mg ml⁻¹ using a 100 kDa molecular weight cut-off centrifugal concentrator (Millipore). The protein purity was checked by SDS-PAGE, and the protein yield and monodispersity were estimated by analytical size exclusion chromatography (aSEC).

Crystals for SWSX were grown using high-throughput nanovolume LCP crystallization. The purified and concentrated protein solution was combined with a lipid mixture: 90% monoolein (Sigma), 10% cholesterol (Affymetrix) in the ratio of 2:3 v/v and homogenized using a lipid syringe mixer until a transparent gel-like LCP

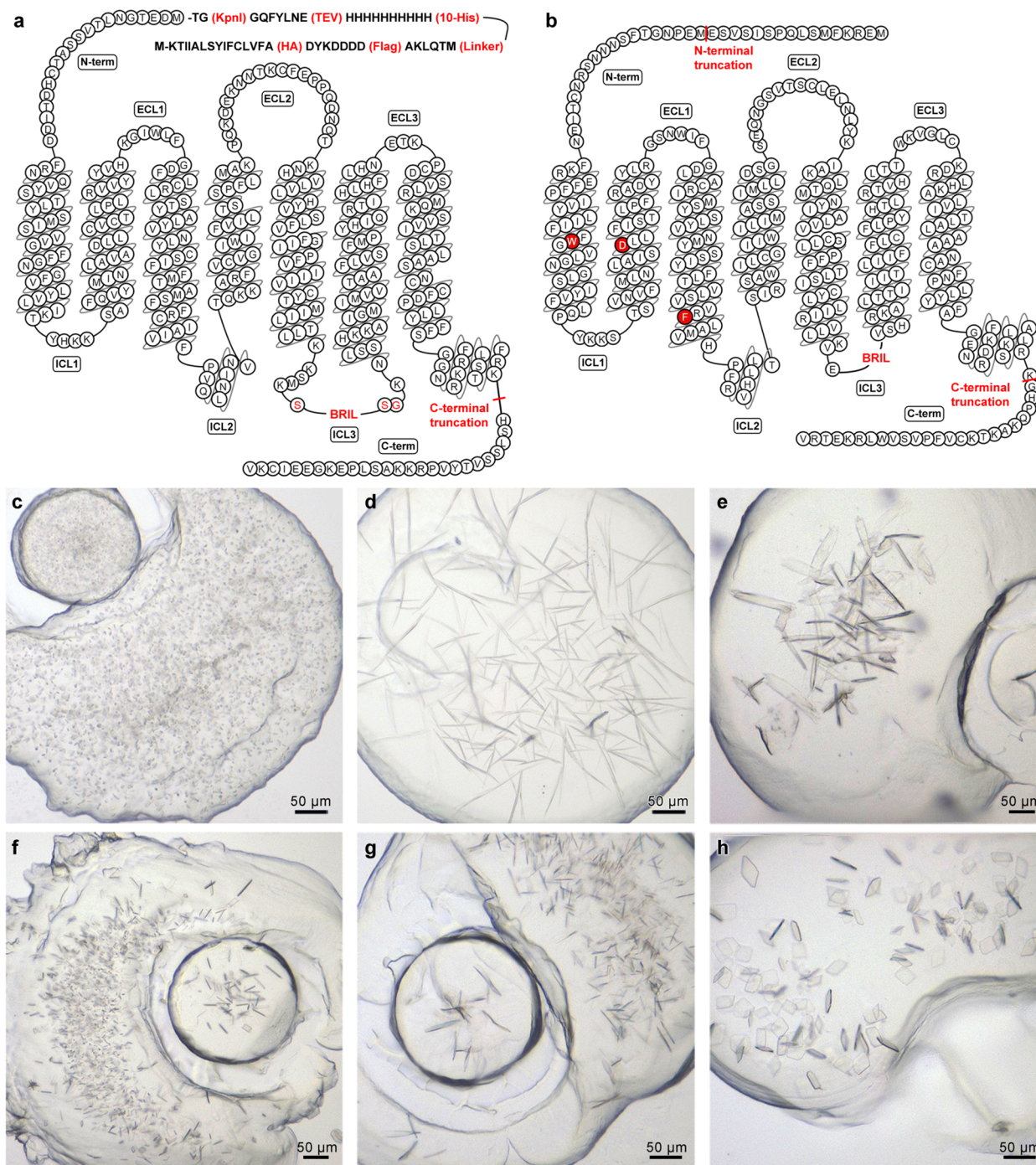


Fig. 1 Construct design and crystallization of CysLT₁R and CysLT₂R. **(a,b)** Amino acid sequence snake-plot of the CysLT₁R **(a)** and CysLT₂R **(b)** crystallization constructs. Protein modifications are shown in red, red background shows stabilising point mutations, red font amino acids – linkers for BRIL insertion. Initial figure drawn using GPCRdb⁴⁹. The N-terminal peptide fragment **(a)** was added to both constructs. **(c–h)** microphotographs of typical crystals grown in lipidic cubic phase (LCP) for CysLT₁R-zafirlukast **(c)**, CysLT₁R-pranlukast **(d)**, and CysLT₂R with antagonists: 11a (C222₁ space group) **(e)**, 11a (F222 space group) **(f)**, 11b **(g)**, and 11c **(h)** complexes⁵¹.

formed³³. Crystallisation was set up in 96-well glass sandwich LCP plates (Marienfeld), with 40 nL LCP drops and 800 nL precipitant drops, which were pipetted using an NT8-LCP robot (Formulatrix). All LCP manipulations were performed at room temperature (20–23 °C), and plates were incubated and imaged at 22 °C using an automated incubator/imager RockImager 1000 (Formulatrix).

CysLT₁R-pranlukast crystals had a needle shape (Fig. 1d) and gained their full size after 3–4 weeks; however, the best diffraction was obtained from samples incubated for 2 months. CysLT₂R crystals grew to their full size

within 1–3 weeks. Crystals of CysLT₂R in complex with ligands 11a and 11b had a shape of an elongated plate with a maximal size up to 150 μm (Fig. 1e–g). In case of CysLT₂R-11c complex, crystals grew as flat parallelepipeds as long as 30–50 μm in diagonal (Fig. 1h). For the full list of crystallization conditions for crystals used in the data collection see Table 1.

Microcrystals of the CysLT₁R-zafirlukast complex for SFX were grown in 100 μl gas-tight Hamilton syringes as previously described^{34,35}. Briefly, approximately 5 μl of protein-laden LCP was transferred through a coupler (Formulatrix) into a syringe, containing 50 μl of precipitant, so that LCP extends towards the plunger as a straight filament. For experiments conducted in 2016 (dataset CysLT1R_zafirlukast-P21), zafirlukast was added at 50 μM prior to the protein concentration. Crystals grew in the following precipitant conditions: 100 mM ammonium phosphate, 31–34% v/v PEG400, 100 mM HEPES pH 7.0, 1 μM zafirlukast. For experiments conducted in 2017 (dataset CysLT1R_6RZ5), zafirlukast was added at 200 μM prior to the protein concentration. Crystals grew in the following precipitant conditions: 120–200 mM sodium/potassium phosphate, 31–34% v/v PEG400, 100 mM HEPES pH 7, no zafirlukast added. Crystals grew for 1–2 weeks, reaching an average crystal size of 5 × 2 × 2 μm (Fig. 1c).

Synchrotron data collection. *Crystal harvesting.* Crystals were harvested directly from LCP using 50–200 μm dual thickness MicroMounts or 400–700 μm MicroMesh loops (MiTeGen) with various hole sizes and flash frozen in liquid nitrogen, as described³⁶.

Full sets data collection. Single-crystal datasets (for CysLT1R_6RZ4 and CysLT2R_6RZ8) were collected using the following procedure. First, the best diffracting position was found using automatic X-ray centring³⁷ with a microfocus beam, followed by characterization³⁷ and dose estimation using BEST³⁸ software, and further data collection as proposed by BEST. This resulted in over 90% complete datasets, however, with a relatively low resolution (>3 Å).

Partial sets data collection. To improve resolution, SWSX partial datasets (minisets, as introduced by Basu *et al.*³⁰) were collected using an updated version of the raster-scanning approach³⁹. The process is illustrated in Fig. 2a. Each loop was first visually aligned and oriented with its plane perpendicular to the X-ray beam. Then, the whole loop was scanned with the beam to identify locations with diffracting crystals (shutterless mode was used on the ID29 and ID30b beamlines). Raster scans were performed using a minimal dose per image, which allowed for visual detection of diffraction spots, but was less than 1% of the total dose per dataset. The grid spacing was set around $\sqrt{2}R$, where R is the beam profile radius (HWHM). The overlap between adjacent beam spots was introduced to improve accuracy in location of the best diffracting positions and to maximize the grid coverage by HWHM profiles. The grid cells showing diffraction spots were ranked by the DOZOR score³⁷ and then manually selected for further data collection. In the case of large single crystals spanning through several grid cells, minisets were collected starting from the highest ranked location and then moving to the next best location along the crystal but skipping grid cells if they had a common edge with the cells already used for data collection to avoid collecting data from previously exposed parts of the crystal. Consecutive minisets from the same crystal were collected by ensuring 1–2° overlaps in the goniometer rotation ω angle. When the goniometer rotation angle exceeded 10° from its original orientation, a new line raster scan was performed to re-align the crystal with the beam. Each miniset was collected restricting an estimated dose per diffraction location within ~20 MGy and using 0.1–0.2° oscillation and 3–20° total wedge size. The wedge size and the corresponding exposure time were selected based on the total number of harvested crystals from the particular condition and were adjusted by decreasing the wedge size and increasing the exposure time when preliminary data processing indicated that a complete dataset had been already collected, or in case of a weak diffraction. The beam size was chosen to match the smallest crystal dimension. A summary of miniset parameters for each SWSX entry is given in Table 2.

XFEL data collection. *Loading crystals into injector.* Precipitant solutions were slowly withdrawn from 3 syringes containing microcrystals of appropriate size and density through a 22 s gauge Hamilton needle. The remaining samples of LCP with microcrystals embedded in it were consolidated from these 3 syringes into one syringe using a syringe coupler (Formulatrix). An aliquot of ~10% of 7.9 MAG lipid was added to the sample to absorb the excess of the precipitant and to avoid LCP freezing upon extrusion in the vacuum chamber⁴⁰. A total sample volume of 15–20 μl was loaded into an LCP injector as described⁴⁰.

LCLS data collection: 2016. An overall scheme of the data collection setup is shown in Fig. 2b. SFX data of CysLT1R_Zafirlukast-P21 were collected in August 2016 at the CXI instrument of the Linac Coherent Light Source (LCLS) at the SLAC National Accelerator Laboratory, Menlo Park, California. LCLS was operated at a wavelength of 1.305 Å (9.50 keV) delivering individual X-ray pulses of 40 fs duration and 2.6×10^{10} photons per pulse focused into a spot size of ~1.5 μm in diameter using a pair of Kirkpatrick-Baez mirrors. LCP with protein microcrystals was extruded at room temperature and at a flow rate of 0.3 μl min⁻¹ inside a vacuum chamber into the beam focus region using an LCP injector⁴⁰ with a 50-μm diameter capillary. The XFEL beam was attenuated at transmission levels of 6.1% to avoid disruptions of the LCP stream. Diffraction images were collected at an XFEL pulse repetition rate of 120 Hz using a 2.3 Megapixel Cornell-SLAC Pixel Array Detector⁴¹ (CSPAD).

A total number of 900,173 detector images were collected, of which 22,047 (2% of total) were identified as potential crystal hits with more than 15 Bragg peaks with SNR = 6.0, threshold 100 and min-pix-count 3.0 using peakfinder8 algorithm as implemented in Cheetah⁴². The overall time of data collection from a sample with a total volume of 27 μl was about 2 h 6 min.

Dataset	Condition ID	No. minisets	Condition
CysLT1R_6RZ4	1	27	100 mM Tris pH8, 33% PEG400, 160 mM Sodium Nitrate, 1% v/v 1,2-Butanediol
	2	4	100 mM Tris pH8, 34% PEG400, 130 mM Sodium Nitrate
	3	40	100 mM Tris pH8, 34% PEG400, 75 mM Sodium Nitrate
	4	8	100 mM Sodium Citrate pH6, 31% PEG400, 200 mM Lithium Nitrate
	5	23	100 mM Tris pH8, 33% PEG400, 160 mM Sodium Nitrate, 4% v/v 2,5-Hexanediol (mixture of isomers)
	6	23	100 mM Sodium Citrate pH6, 34% PEG400, 400 mM Lithium Nitrate, 10 mM Betaine hydrochloride
	7	13	100 mM Tris pH8, 34% PEG400, 266 mM Sodium Nitrate
	8	5	100 mM Sodium Citrate pH6, 34% PEG400, 400 mM Lithium Nitrate, 3% w/v D-(+)-Glucose monohydrate
	9	2	100 mM Sodium Citrate pH6, 34% PEG400, 400 mM Lithium Nitrate, 100 mM Cesium Chloride
	10	2	100 mM Tris pH8.2, 37% PEG400, 200 mM Sodium Nitrate, 4% v/v 2,5-Hexanediol (mixture of isomers)
	11	16	100 mM Sodium Citrate pH6, 34% PEG400, 400 mM Lithium Nitrate, 4% v/v 2,5-Hexanediol (mixture of isomers)
	12	11	100 mM Tris pH8, 33% PEG400, 160 mM Sodium Nitrate, 10 mM Spermine tetrahydrochloride
	13	7	100 mM Sodium Citrate pH6, 30% PEG400, 200 mM Lithium Nitrate
	14	2	100 mM Sodium Citrate pH6, 30% PEG400, 236 mM Lithium Nitrate
	15	1	100 mM Tris pH8, 33% PEG400, 160 mM Sodium Nitrate, 10 mM Spermidine
	16	2	100 mM Tris pH8, 33% PEG400, 160 mM Sodium Nitrate, 0.5% w/v n-Dodecyl-b-D-maltoside
CysLT2R_6RZ6	1	9	100 mM Ammonium Sulfate, 30% v/v PEG400, 100 mM HEPES pH7.0
	2	6	130 mM Ammonium Tartrate dibasic, 30% v/v PEG400, 100 mM HEPES pH 7.0, 10 mM Spermine tetrahydrochloride
	3	12	100 mM Ammonium Sulfate, 30% v/v PEG400, 100 mM HEPES pH7.0
	4	2	100 mM Lithium Sulfate monohydrate, 30% v/v PEG400, 100 mM HEPES pH7.0
	5	18	30 mM Ammonium Tartrate dibasic, 20% v/v PEG400, 100 mM HEPES pH 7.0, 10 mM Betaine hydrochloride
	6	7	60 mM Ammonium Tartrate dibasic, 22% PEG400, 100 mM HEPES pH7.0
	7	19	70 mM Ammonium Tartrate dibasic, 22% PEG400, 100 mM HEPES pH7.0
	8	2	30 mM Ammonium Tartrate dibasic, 20% PEG400, 100 mM HEPES pH7.0
	9	7	100 mM Ammonium Tartrate dibasic, 30% v/v PEG400, 100 mM TRIS pH8.0
	10	9	100 mM Ammonium Tartrate dibasic, 24% PEG400, 100 mM HEPES pH7.0
	11	1	100 mM Ammonium Tartrate dibasic, 26% PEG400, 100 mM HEPES pH7.0
	12	1	120 mM Ammonium Tartrate dibasic, 26% PEG400, 100 mM HEPES pH7.0
	13	7	120 mM Ammonium Tartrate dibasic, 28% PEG400, 100 mM HEPES pH7.0
	14	4	100 mM Ammonium Tartrate dibasic, 30% v/v PEG400, 100 mM TRIS pH8.0
	15	17	100 mM Ammonium Tartrate dibasic, 30% v/v PEG400, 100 mM TRIS pH8.0
	16	52	80 mM Ammonium Tartrate dibasic, 24% PEG400, 100 mM HEPES pH7.0
	17	5	130 mM Ammonium Tartrate dibasic, 30% v/v PEG400, 100 mM HEPES pH 7.0, 10 mM Yttrium(III) Chloride hexahydrate
	18	20	100 mM Ammonium Tartrate dibasic, 26% PEG400, 100 mM HEPES pH7.0
	19	3	130 mM Ammonium Tartrate dibasic, 26% PEG400, 100 mM HEPES pH7.0
	20	2	130 mM Ammonium Tartrate dibasic, 28% PEG400, 100 mM HEPES pH7.0
	21	1	30 mM Ammonium Tartrate dibasic, 20% v/v PEG400, 100 mM HEPES pH 7.0, 0.025% v/v Dichloromethane
	22	1	90 mM Ammonium Tartrate dibasic, 24% PEG400, 100 mM HEPES pH7.0
	23	6	30 mM Ammonium Tartrate dibasic, 20% v/v PEG400, 100 mM HEPES pH 7.0, 1% v/v 1,2-Butanediol
	24	9	30 mM Ammonium Tartrate dibasic, 20% v/v PEG400, 100 mM HEPES pH 7.0, 4% v/v 1-Propanol
25	11	130 mM Ammonium Tartrate dibasic, 27.4% PEG400, 100 mM HEPES pH7.0	
26	5	120 mM Ammonium Tartrate dibasic, 26% PEG400, 100 mM HEPES pH7.0	
CysLT2R_6RZ7	1	2	130 mM Ammonium Tartrate dibasic, 30% v/v PEG400, 100 mM HEPES pH 7.0, 0.025% v/v Dichloromethane
	2	4	100 mM Ammonium Tartrate dibasic, 30% v/v PEG400, 100 mM TRIS pH8.0
	3	10	100 mM Ammonium Tartrate dibasic, 24% PEG400, 100 mM HEPES pH7.0
	4	9	100 mM Ammonium Sulfate, 30% v/v PEG400, 100 mM HEPES pH7.0

Continued

Dataset	Condition ID	No. minisets	Condition
	5	18	30 mM Ammonium Tartrate dibasic, 20% v/v PEG400, 100 mM HEPES pH 7.0, 10 mM Betaine Hydrochloride
	6	9	30 mM Ammonium Tartrate dibasic, 20% v/v PEG400, 100 mM HEPES pH 7.0, 4% v/v 1-Propanol
	7	8	130 mM Ammonium Tartrate dibasic, 30% v/v PEG400, 100 mM HEPES pH 7.0, 10 mM Yttrium(III) Chloride hexahydrate
	8	3	100 mM Lithium Sulfate monohydrate, 30% v/v PEG400, 100 mM HEPES pH7.0
	9	1	120 mM Ammonium Tartrate dibasic, 26% PEG400, 100 mM HEPES pH7.0
	10	6	110 mM Ammonium Tartrate dibasic, 26% PEG400, 100 mM HEPES pH7.0
	11	1	30 mM Ammonium Tartrate dibasic, 20% v/v PEG400, 100 mM HEPES pH 7.0, 0.025% v/v Dichloromethane
	12	16	120 mM Ammonium Tartrate dibasic, 28% PEG400, 100 mM HEPES pH7.0
	13	14	130 mM Ammonium Tartrate dibasic, 28% PEG400, 100 mM HEPES pH7.0
	14	6	30 mM Ammonium Tartrate dibasic, 20% v/v PEG400, 100 mM HEPES pH 7.0, 1% v/v 1,2-Butanediol
	15	16	30 mM Ammonium Tartrate dibasic, 20% PEG400, 100 mM HEPES pH7.0
	16	23	130 mM Ammonium Tartrate dibasic, 27.4% PEG400, 100 mM HEPES pH7.0
	17	6	100 mM Ammonium Tartrate dibasic, 30% v/v PEG400, 100 mM TRIS pH8.0
	18	6	130 mM Ammonium Tartrate dibasic, 30% v/v PEG400, 100 mM HEPES pH 7.0, 10 mM Spermine tetrahydrochloride
CysLT2R_6RZ8	1	11	100 mM Potassium fluoride, 30% v/v PEG400, 100 mM TRIS pH8.0
CysLT2R_6RZ9	1	18	210 mM Ammonium Tartrate dibasic, 30.9% PEG400, 100 mM HEPES pH7.0
	2	4	100 mM Ammonium Tartrate dibasic, 30% v/v PEG400, 100 mM TRIS pH8.0
	3	3	80 mM Ammonium Tartrate dibasic, 29.14% PEG400, 100 mM HEPES pH7.0
	4	5	20 mM Ammonium Tartrate dibasic, 32.6% PEG400, 100 mM HEPES pH7.0
	6	8	250 mM Ammonium Tartrate dibasic, 32.6% PEG400, 100 mM HEPES pH7.0
	7	2	130 mM Ammonium acetate, 27.4% PEG400, 100 mM HEPES pH7.0
	8	2	50 mM Ammonium Tartrate dibasic, 34.9% PEG400, 100 mM HEPES pH7.0
	9	2	90 mM Ammonium Tartrate dibasic, 29.14% PEG400, 100 mM HEPES pH7.0

Table 1. Summary of crystallization conditions for SWSX datasets.

LCLS data collection: 2017. SFX data of CysLT1R_6RZ5 were collected in August 2017 at the CXI instrument. LCLS was operated at a wavelength of 1.302 Å (9.52 keV) delivering individual X-ray pulses of 43 fs duration and 1.9×10^{10} photons per pulse focused into a spot size of $\sim 1.5 \mu\text{m}$ in diameter using a pair of Kirkpatrick-Baez mirrors. LCP with protein microcrystals was extruded at room temperature and at a flow rate of $0.3 \mu\text{l min}^{-1}$ inside a vacuum chamber into the beam focus region using an LCP injector⁴⁰ with a 50- μm diameter capillary. The XFEL beam was attenuated at transmission levels of 6.3–10% to avoid disruptions of the LCP stream. Diffraction images were collected at an XFEL pulse repetition rate of 120 Hz using a 2.3 Megapixel Cornell-SLAC Pixel Array Detector⁴³ (CSPAD).

A total number of 390,442 detector images were collected, of which 43,417 (11% of total) were identified as potential crystal hits with more than 20 Bragg peaks with SNR = 4.0, threshold 200 and min-pix-count 3.0 using peakfinder8 algorithm as implemented in Cheetah⁴². The overall time of data collection from a sample with a total volume of $15 \mu\text{l}$ was about 54 min.

Data processing. All datasets, except for the SFX dataset CysLT1R_Zafirlukast-P21 (P21 space group), have been previously indexed, integrated, sorted, and merged to solve the structures of the corresponding receptor complexes by molecular replacement, as described^{28,29}. Re-processing of the data with the same or better processing statistics as in the original manuscripts is described in the *Technical validation* section.

Data Records

SWSX data^{44–49} have been deposited to Zenodo under accession numbers provided in Table 3. Each SWSX dataset folder contains subfolders, representing each miniset collected, regardless of the angular range for data collection. Each miniset subfolder is named as XXX_YY_ZZ_NN, where XXX is the sequential number of the miniset, YY is the crystallization condition ID, ZZ is the serial number of the harvesting loop within each crystallization condition, NN – the serial number of the miniset within each loop. Each miniset subfolder contains a subfolder ‘images’ with all diffraction images in either cbf or HDF5 format. It also contains an XDS parameter file XDS.INP with the keyword NAME_TEMPLATE_OF_DATA_FRAMES pointing to files in ‘images’ subfolder, and other parameters as used during reprocessing (see keywords for express.py below). Also, each miniset subfolder contains all XDS-related files (including geometry correction x_geo_corr.cbf and y_geo_corr.cbf for cbf files) for this miniset (everything up to CORRECT.LP and XDS_ASCII.HKL for successfully integrated datasets, and only COLSPOT.LP for non-successful ones). A summary of all SWSX entries is shown in Table 2, and a summary of all SWSX entries crystallization conditions is present in Table 1, with a full description provided in Supplementary Table 1.

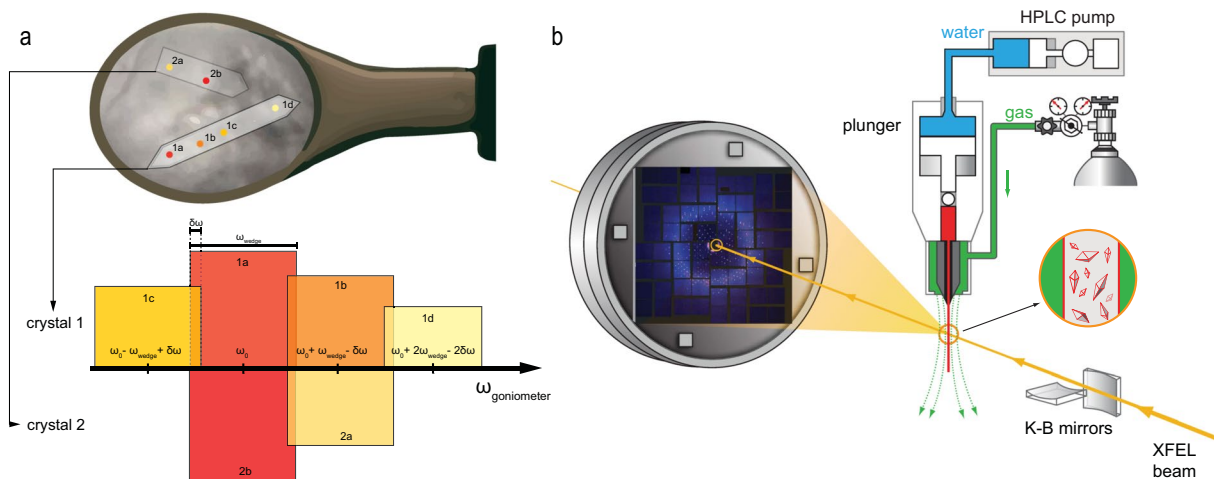


Fig. 2 Synchrotron and XFEL data collection setups. (a) Schematics of the SWSX data collection process. The bar colour indicates the DOZOR score (from red – the best diffraction, to yellow – the worst). For minisets collected from the same crystal, as judged by the diffraction patterns and DOZOR score heatmap, an overlap of $\delta\omega = 1-2^\circ$ is introduced between consecutive sets. When the rotation angle ω exceeds $\sim 10^\circ$ from the initial orientation, as for the point 1d, an additional line scan is performed to re-align the crystal. The orientations of two different crystals 1 and 2 in the loop are assumed independent, and thus minisets from them are collected within the same ω range. (b) LCP-SFX data collection scheme. Microcrystals embedded in LCP are injected inside a vacuum chamber into the XFEL beam focus region using a viscous media microextrusion injector. A stream of sheath gas (nitrogen or helium) is used to keep the LCP stream straight. Microcrystals intersect with the XFEL beam in random orientations and diffraction patterns are collected by a CSPAD detector.

Entry	CysLT1R_6RZ4	CysLT2R_6RZ6	CysLT2R_6RZ7	CysLT2R_6RZ9	CysLT2R_6RZ8
Reported resolution, Å	2.7	2.43	2.43	2.73	2.7
Reprocessed resolution, Å	2.6	2.43	2.43	2.73	2.5
No. collected minisets	186	236	158	44	11
No. processed minisets	116	126	144	38	11
No. minisets in the final dataset	9	74	16	12	8
Wedge size, °	10–180	3–12	4–20	10–20	10–20
Detector/beamline	Eiger-4M/ID30a3 Pilatus3-S-6M/ID30b Pilatus-6M/ID29	Pilatus3-S-6M/ID30b Pilatus-6M/ID29	Eiger-4M/ID30a3 Pilatus-6M/ID23-1 Pilatus-6M/ID29	Pilatus-6M/ID23-1 Pilatus-6M/ID29	Pilatus-6M/ID23-1

Table 2. Summary of SWSX datasets.

Entry	Reported resolution in PDB, Å	No. minisets (SWSX) or No. indexed lattices (SFX)	Entry page	Entry size
CysLT2R_6RZ6	2.43	236 (SWSX)	https://zenodo.org/record/4032836	48.2 GB
CysLT2R_6RZ7	2.43	158 (SWSX)	https://zenodo.org/record/4032837	88.1 GB
CysLT2R_6RZ9	2.73	11 (SWSX)	https://zenodo.org/record/4032841	18.7 GB
CysLT2R_6RZ8	2.70	44 (SWSX)	https://zenodo.org/record/4032840	8.9 GB
CysLT1R_6RZ4	2.70	186 (SWSX)	https://zenodo.org/record/4032826	90.0 GB
CysLT1R_6RZ5	2.53	43,417 (SFX)	https://www.cxidb.org/id-106.html	134.9 GB
CysLT1R_Zafirlukast-P21	N/A	22,047 (SFX)	https://www.cxidb.org/id-107.html	193.6 GB

Table 3. Data availability on Internet. Github gist, associated with the publication, has the ‘download_all.sh’ script for Linux to download all data entries described in this publication.

SFX data have been deposited to CXIDB as ID106⁵⁰ (CysLT1R_6RZ5) and ID107⁵¹ (CysLT1R_Zafirlukast-P21). Only those images identified as crystal hits by Cheetah are included in the deposited dataset. Each SFX dataset folder contains a subfolder ‘raw_data’ with all runs as written by Cheetah, their respective cheetah.ini files and cxi files with images. Also, each SFX dataset folder contains a file ‘initial.geom’ that was used during reprocessing. A summary for all SFX entries is given in Table 4.

Entry	CysLT1R_6RZ5	CysLT1R_Zafirlukast-P21
Reported resolution, Å	2.53	N/A
Reprocessed resolution, Å	2.50	3.5
Total No. images	390,442	900,173
No crystal hits	43,417	22,047
No. indexed images	28,528	17,193
No. indexed lattices	28,900	17,193

Table 4. Summary of SFX datasets.

PDB ID	CysLT1R			CysLT2R			
	6RZ4	6RZ5	Zafirlukast-P21	6RZ6	6RZ7	6RZ9	6RZ8
Dataset type	SWSX	SFX	SFX	SWSX	SWSX	SWSX	SWSX
No. crystals (SFX) or No. minisets (SWSX)	9	28,900	17,193	74	16	12	8
Cell dimensions							
<i>a b c</i> , Å	59.39 45.89 87.13	41.58 68.56 87.37	43.86 159.43 73.48	69.34 167.95 85.44	81.82 142.07 171.21	67.67 165.01 82.66	78.40 78.40 171.91
$\alpha \beta \gamma$, °	90.00 95.69 90.00	76.33 76.69 81.19	90.00 95.12 90.00	90.00 90.00 90.00	90.00 90.00 90.00	90.00 90.00 90.00	90.00 90.00 90.00
Space group	P2 ₁	P1	P2 ₁	C22 ₂₁	F222	I4	C22 ₂₁
Resolution, Å [#]	30.0-2.6 (2.67-2.60)	30.0-2.53 (2.57-2.53)	30.0-3.5 (3.56-3.50)	30.0-2.3 (2.36-2.30)	30.0-2.43 (2.49-2.43)	30.0-2.5 (2.56-2.50)	30.0-2.73 (2.80-2.73)
Completeness, % [#]	99.9 (100.0)	100.0 (100.0)	100.0 (100.0)	99.2 (97.6)	98.2 (98.0)	99.9 (100.0)	94.7 (95.4)
Redundancy [#]	7.24 (6.86)	67.6 (31.0)	128.7 (73.6)	7.39 (5.80)	6.15 (6.25)	12.5 (12.8)	3.27 (3.35)
R _{meas} (SWSX) or R _{split} (SFX) [#]	0.35 (1.05)	0.23 (2.80)	0.16 (2.59)	0.30 (2.74)	0.31 (3.33)	0.24 (5.52)	0.23 (3.06)
I/σ(I) [#]	5.59 (1.93)	2.89 (0.42)	4.17 (0.46)	5.75 (0.84)	5.48 (0.79)	8.62 (0.67)	3.72 (0.69)
CC [#]	1.00 (0.57)	0.99 (0.51)	1.00 (0.61)	1.00 (0.65)	1.00 (0.63)	1.00 (0.50)	1.00 (0.57)

Table 5. Crystallographic data collection statistics. [#]Values in parentheses are for highest-resolution shell.

Entry		CysLT2R_6RZ6	CysLT2R_6RZ7	CysLT2R_6RZ9	CysLT2R_6RZ8	CysLT1R_6RZ4
Low-resolution rejection	Resolution limits, Å/No. bins	N/A	N/A	30.0-10.0/17	30.0-10.0/7	32.0-10.0/5
	Δ CC _{1/2} threshold	N/A	N/A	0.0	1.0	2.0
	No. iterations	0	0	5	5	4
High-resolution rejection	Resolution limits, Å/No. bins	30.0-2.3/23	30.0-2.43/23	30.0-2.73/17	10.0-2.5/15	5.0-2.6/15
	Δ CC _{1/2} threshold	3.0	3.0	5.0	1.0	2.0
	No. iterations	5	5	7	4	5

Table 6. SWSX data processing parameters. For CysLT2R_6RZ6 and CysLT2R_6RZ7, only full resolution range rejection was performed.

Technical Validation

Data processing. During the preparation of this manuscript, all data were re-processed in a consistent manner. Here we present a pipeline for data processing that results in similar or better resolution values and figures of merit compared to those reported in the original papers. Data processing statistics for all datasets is shown in Table 5.

SWSX data. For SWSX data, the processing algorithm works as following (note that the treatment of both full datasets and minisets is the same). For each dataset, initial indexing and integration are performed by XDS within the resolution range of 40–2.5 Å using the beamline-provided XDS.INP file, without specifying the unit cell parameters and the space group identity (for Dectris images, the “neugia” library was used, as described here (<https://strucbio.biologie.uni-konstanz.de/xds/wiki/index.php/Eiger>)). Each integration runs first with the keywords “JOB = XCORR INIT COLSPOT IDXREF DEFPIX INTEGRATE CORRECT”, then the integration parameters are updated using the output of the CORRECT step as described in the section “Final polishing: Re-INTEGRATEing with the correct spacegroup, refined geometry and fine-slicing of profiles” (https://strucbio.biologie.uni-konstanz.de/xds/wiki/index.php/Optimisation#Re-INTEGRATEing_with_the_correct_spacegroup.2C_refined_geometry_and_fine-slicing_of_profiles), and integration is re-run using the keywords “JOB = DEFPIX INTEGRATE CORRECT”. After that, the algorithm attempts to scale all obtained XDS_ASCII.HKL files using XSCALE, and runs several rounds of Δ CC_{1/2} rejection of non-isomorphous minisets using xdscc12 subprogram as described¹⁷ (until there are no rejected minisets at the subsequent iteration). For most

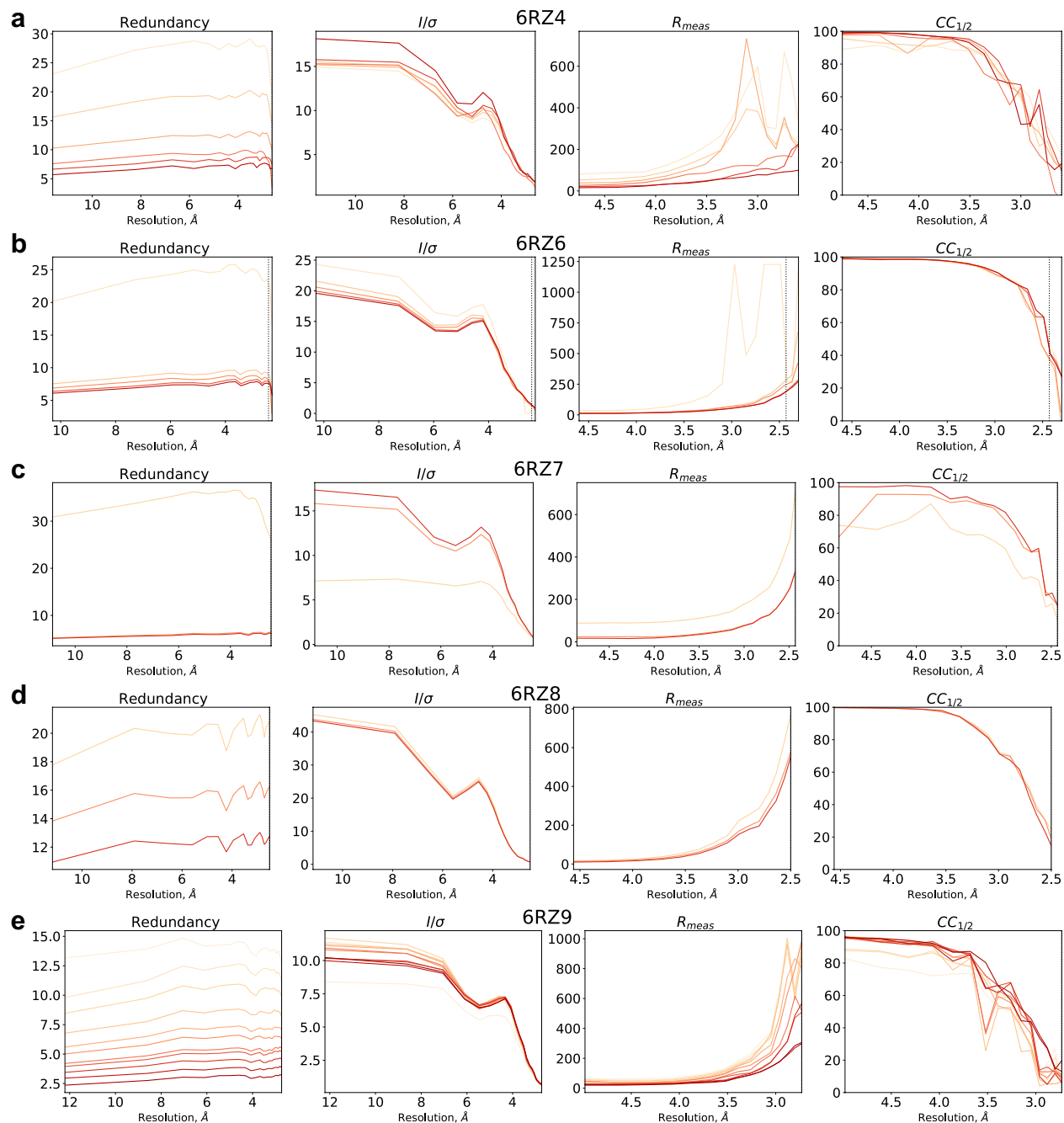


Fig. 3 Improvements in data merging statistics for SWSX datasets during $\Delta CC_{1/2}$ rejection process. (a–e) Plots of redundancy, I/σ , R_{meas} and $CC_{1/2}$ vs resolution for each data processing iteration are shown for the following datasets: CysLT1R_6RZ4 (a), CysLT2R_6RZ6 (b), CysLT2R_6RZ7 (c), CysLT2R_6RZ8 (d), CysLT2R_6RZ9 (e). Darker curves represent latter stages of $\Delta CC_{1/2}$ miniset rejection.

datasets, the miniset rejection was applied in two steps: first, using the low-resolution range (e.g. 30.0–10.0 Å, $\Delta CC_{1/2}$ threshold 0–2), and then using the high-resolution range (e.g. 10.0–2.5 Å, $\Delta CC_{1/2}$ threshold 1–5). All processing parameters are summarized in Table 6. The obtained dataset is merged and used as a REFERENCE_DATA_SET during the 2nd integration attempt of all minisets (including those rejected during the previous integration attempts). If $CC_{1/2}$ in the highest resolution shell exceeds 0.15, the RESOLUTION_RANGE is increased manually for the 3rd integration. Next, another round of $\Delta CC_{1/2}$ rejection of non-isomorphous minisets is performed followed by merging to produce a final dataset. Improvements in the figures of merit for a dataset as a result of $\Delta CC_{1/2}$ rejection are shown in Fig. 3. For the CysLT2R_6RZ8 dataset (space group I4), there is an indexing ambiguity with two indexing options available for each miniset, thereby some minisets have to be re-indexed using 'REIDX_ISET = 0 -1 0 0 -1 0 0 0 0 -1 0' keyword in XSCALE. This is done by following an iterative procedure: first, two largest minisets are merged together using two possible indexing options for the second set, and

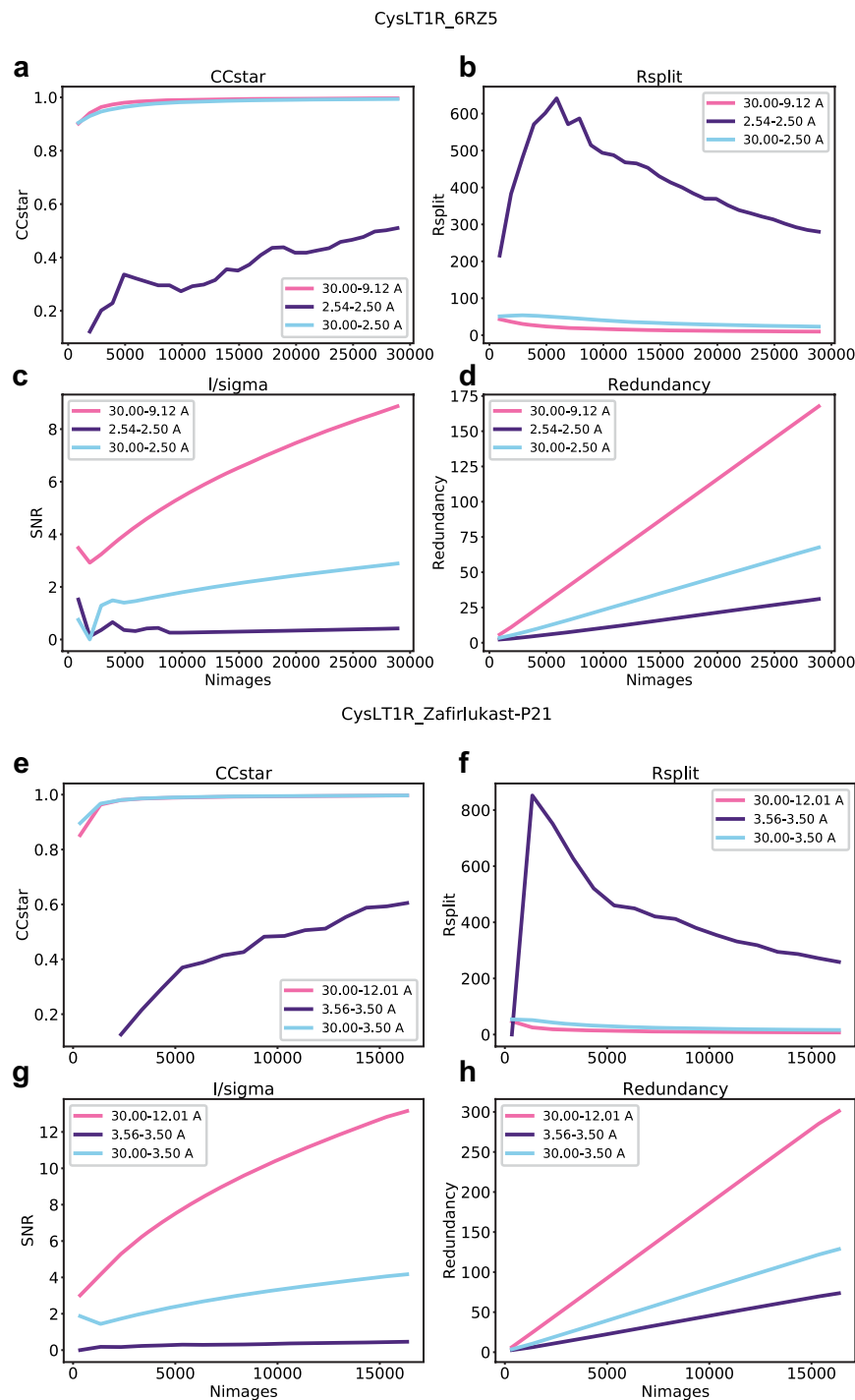


Fig. 4 Improvements in SFX data processing statistics with increasing the number of crystals. (**a–d**) Plots of I/σ (**a**), R_{split} (**b**), CC^* (**c**) and redundancy (**d**) in three major resolution shells (low resolution, high resolution and overall) vs the number of crystals used for merging for the dataset CysLT1R_6RZ5. (**e–h**) The same as panels (**a–d**) but for the dataset CysLT1R_Zafirlukast_P21.

the indexing option resulting in a smaller R_{meas} is chosen. Then, all other minisets are added one by one, using the indexing choice that produces smaller R_{meas} for the merged dataset. For the final merged dataset, phenix.xtriage reports no significant twinning.

SFX data. CysLT1R_6RZ5. Previously published data²⁸ were processed using CrystFEL (v. 0.6.3 + 23ea03c7). For peak finding, peakfinder8 with min-snr = 4.5, threshold = 210 was used. For indexing, the following indexers were employed: felix, dirax, asdf, taketwo, mosflm-nolatt-cell, mosflm-nocell-latt, and xds (in that order), with-multi option enabled. Data were merged using process_hkl, with push-res = 1.8 and max-adu = 14,000.

For reprocessing, the same parameters in CrystFEL (v. 0.8.0) were used. The final reprocessed dataset included 28,900 indexed lattices (67% of the frames selected by Cheetah). Among indexers, felix was the most successful one, providing 16,717 indexed lattices (57.8% of all indexed lattices). Improvements of R_{split} , CC^* and I/σ are shown in Fig. 4a–d.

CysLT1R_Zafirlukast-P21. Data (previously unpublished) were processed using CrystFEL (v. 0.8.0). For peak finding, peakfinder8 with $\text{highres} = 3.0$, $\text{min-snr} = 4.4$, $\text{threshold} = 20$, $\text{max-res} = 300$ and $\text{min-res} = 80$ was used. For indexing, indexers dirax, taketwo, mosflm, xds, and asdf (in that order) were used. Data were merged using process_hkl, with $\text{mincc} = 0.3$ and $\text{push-res} = 5.0$. The final dataset resulted in 17,193 indexed lattices (79% of the frames selected by Cheetah). Among indexers, dirax was the most successful one, providing 14,457 indexed lattices. Improvements of R_{pim} , CC^* and I/σ are shown in Fig. 4e–h.

Usage Notes

Downloading data. The information about downloading data is shown in Table 3. A Linux script ‘download_all.sh’, fetching all data using *curl* utility is provided on the Github gist, associated with the publication. Folder with each entry is archived in a single tar.gz file for more convenient fetching.

Data processing assistance scripts. Here, a brief description of scripts is given. Please, find a more detailed description in the github gist (<https://gist.github.com/marinegor/96102c9b7ce87509a0832649d11ba927>), associated with the publication.

1. create_xscale.inp.py — a simple script to include all existing XDS_ASCII to XSCALE.INP
Given the structure of folders as in data deposited in this publication, creates an input file for express.py in the csv format
2. express.py — the SWSX integration pipeline
Given a list of folders with XDS.INP and a path to the respective data sets, the script runs XDS for all data sets in the list, optionally adding UNIT_CELL_CONSTANTS, SPACE_GROUP_NUMBER, INCLUDE_RESOLUTION_RANGE, setting SPOT_RANGE same as DATA_RANGE, and setting REFERENCE_DATA_SET. Adds MAXIMUM_NUMBER_OF_PROCESSORS and MAXIMUM_NUMBER_OF_JOBS for processing on large clusters. Runs xscale_par afterwards.
3. xdsc.py — parsing of XDSCC.LP logfile of *xdsc12* utility for rejection of minisets based on $\Delta CC_{1/2}$.
Analyses the output of *xdsc12* utility together with the last XSCALE.INP used, providing the list of data sets with their $\Delta CC_{1/2}$ values. Saves list of those which have $\Delta CC_{1/2}$ higher than the input threshold value.
4. reject.sh — iterative “until no dataset with negative $\Delta CC_{1/2}$ are left” dataset rejection script
Scales XDS_ASCII.HKL files in all subfolders of the current folder. Then iteratively runs $\Delta CC_{1/2}$ rejection with the given resolution range and the number of cycles. Saves all intermediate XSCALE.INP-s and XSCALE.LP-s.
5. run_crystfel.sh
A wrapper for the *indexamajig* routine, which i) arranges all CrystFEL-related files into subfolders, ii) automatically assigns the date and time for each generated stream and respective log file, iii) links the last created stream to ‘laststream’ link, and shuffles the input file list, so that one could quickly and reliably check the indexing rate before the indexing finishes.
6. analysis.sh
A wrapper for *process_hkl*, *partialator*, *check_hkl*, and *compare_hkl* routines, which produces an XSCALE.LP-like statistics table, counts images indexed with different indexers, produces a command-line visible histogram of the image resolution (for a simple estimation of the push-res parameter), and writes logs.

Code availability

The code used for data reprocessing (see usage notes in *Technical validation* section) is available on github gist (<https://gist.github.com/marinegor/96102c9b7ce87509a0832649d11ba927>). The utility *xdsc12* is available through XDS-Wiki website (<https://strucbio.biologie.uni-konstanz.de/xdswiki/index.php/Xdsc12>). In previous publications, for SFX data processing, CrystFEL version 0.6.3 + 23ea03c7 (available on <https://stash.desy.de/projects/CRYIS/repos/crystfel/commits>) was used. For SWSX data processing, XDS (version BUILT = 20161101 for CysLT1R_6RZ4 and BUILT = 20161205 for CysLT2R_6RZ5–9) and XSCALE (version BUILT = 20161101 for CysLT1R_6RZ4 and BUILT = 20180319 for CysLT2R_6RZ4–9) were used in the original publication, together with the “neggia” library for reading HDF5 images, as described (<https://strucbio.biologie.uni-konstanz.de/xdswiki/index.php/Eiger>). For data reprocessing, XDS and XSCALE version BUILT = 20190315, and CrystFEL 0.8.0, were used.

Received: 10 July 2020; Accepted: 7 October 2020;
Published: 12 November 2020

References

1. Bäck, M. *et al.* International Union of Basic and Clinical Pharmacology. LXXXIV: Leukotriene Receptor Nomenclature, Distribution, and Pathophysiological Functions. *Pharmacol. Rev.* **63**, 539–584 (2011).
2. Singh, R. K., Tandon, R., Dastidar, S. G. & Ray, A. A review on leukotrienes and their receptors with reference to asthma. *J. Asthma* **50**, 922–931 (2013).
3. Shi, Q.-J. *et al.* Intracerebroventricular injection of HAMI 3379, a selective cysteinyl leukotriene receptor 2 antagonist, protects against acute brain injury after focal cerebral ischemia in rats. *Brain Res.* **1484**, 57–67 (2012).

4. Colazzo, F., Gelosa, P., Tremoli, E., Sironi, L. & Castiglioni, L. Role of the Cysteinyl Leukotrienes in the Pathogenesis and Progression of Cardiovascular Diseases. *Mediators Inflamm.* **2017**, 1–13 (2017).
5. Magnusson, C. *et al.* Low expression of CysLT1R and high expression of CysLT2R mediate good prognosis in colorectal cancer. *Eur. J. Cancer* **46**, 826–835 (2010).
6. Magnusson, C. *et al.* Cysteinyl leukotriene receptor expression pattern affects migration of breast cancer cells and survival of breast cancer patients. *Int. J. Cancer* **129**, 9–22 (2011).
7. Tsai, M.-J. *et al.* Cysteinyl Leukotriene Receptor Antagonists Decrease Cancer Risk in Asthma Patients. *Sci. Rep.* **6**, 23979 (2016).
8. Duah, E. *et al.* Cysteinyl leukotriene 2 receptor promotes endothelial permeability, tumor angiogenesis, and metastasis. *Proc. Natl. Acad. Sci.* **116**, 199–204 (2019).
9. Moore, A. R. *et al.* Recurrent activating mutations of G-protein-coupled receptor CYSLTR2 in uveal melanoma. *Nat. Genet.* **48**, 675–680 (2016).
10. Ceraudo, E. *et al.* Uveal Melanoma Oncogene CYSLTR2 Encodes a Constitutively Active GPCR Highly Biased Toward Gq Signaling. *bioRxiv* 1–60, <https://doi.org/10.1101/663153> (2019).
11. Yokomizo, T., Nakamura, M., Shimizu, T., Sasaki, F. & Yokomizo, T. Leukotriene receptors as potential therapeutic targets. *J. Clin. Invest.* **128**, 2691–2701 (2018).
12. Yamamoto, M. *et al.* Protein microcrystallography using synchrotron radiation. *IUCr* **4**, 529–539 (2017).
13. Mishin, A. *et al.* An outlook on using serial femtosecond crystallography in drug discovery. *Expert Opin. Drug Discov.* **14**, 933–945 (2019).
14. Zander, U. *et al.* Merging of synchrotron serial crystallographic data by a genetic algorithm. *Acta Crystallogr. Sect. D Struct. Biol.* **72**, 1026–1035 (2016).
15. Santoni, G., Zander, U., Mueller-Dieckmann, C., Leonard, G. & Popov, A. Hierarchical clustering for multiple-crystal macromolecular crystallography experiments: the ccCluster program. *J. Appl. Cryst.* **50**, 1844–1851 (2017).
16. Foadi, J. *et al.* Clustering procedures for the optimal selection of data sets from multiple crystals in macromolecular crystallography. *Acta Crystallogr. Sect. D Biol. Crystallogr.* **69**, 1617–1632 (2013).
17. Assmann, G., Brehm, W. & Diederichs, K. Identification of rogue datasets in serial crystallography. *J. Appl. Crystallogr.* **49**, 1021–1028 (2016).
18. Hanson, M. A. *et al.* Crystal Structure of a Lipid G Protein-Coupled Receptor. *Science* (80-). **335**, 851–855 (2012).
19. Diederichs, K. Dissecting random and systematic differences between noisy composite data sets. *Acta Crystallogr. Sect. D Struct. Biol.* **73**, 286–293 (2017).
20. Brehm, W. & Diederichs, K. Breaking the indexing ambiguity in serial crystallography. *Acta Crystallogr. Sect. D Biol. Crystallogr.* **70**, 101–109 (2014).
21. Asada, H. *et al.* Crystal structure of the human angiotensin II type 2 receptor bound to an angiotensin II analog. *Nat. Struct. Mol. Biol.* **25**, 570–576 (2018).
22. White, T. A. *et al.* Serial femtosecond crystallography datasets from G-protein-coupled receptors. *Sci. Data* **3**, 160057 (2016).
23. Toyoda, Y. *et al.* Ligand binding to human prostaglandin E receptor EP4 at the lipid-bilayer interface. *Nat. Chem. Biol.* **15**, 18–26 (2019).
24. Kato, H. E. *et al.* Structural mechanisms of selectivity and gating in anion channelrhodopsins. *Nature* **561**, 349–354 (2018).
25. Kim, Y. S. *et al.* Crystal structure of the natural anion-conducting channelrhodopsin GtACR1. *Nature* **561**, 343–348 (2018).
26. Morin, A. *et al.* Collaboration gets the most out of software. *Elife* **2**, 1–6 (2013).
27. Maia, F. R. N. C. The coherent X-ray imaging data bank. *Nature Methods* **9**, 854–855 (2012).
28. Luginina, A. *et al.* Structure-based mechanism of cysteinyl leukotriene receptor inhibition by antiasthmatic drugs. *Sci. Adv.* **5**, eaax2518 (2019).
29. Gusach, A. *et al.* Structural basis of ligand selectivity and disease mutations in cysteinyl leukotriene receptors. *Nat. Commun.* **10**, 5573 (2019).
30. Basu, S. *et al.* Automated data collection and real-time data analysis suite for serial synchrotron crystallography. *J. Synchrotron Radiat.* **26**, 244–252 (2019).
31. Chun, E. *et al.* Fusion partner toolchest for the stabilization and crystallization of G protein-coupled receptors. *Structure* **20**, 967–976 (2012).
32. Ballesteros, J. A. & Weinstein, H. Integrated methods for the construction of three-dimensional models and computational probing of structure-function relations in G protein-coupled receptors. *Methods Neurosci.* **25**, 366–428 (1995).
33. Caffrey, M., Cherezov, V., Caffrey, M. & Cherezov, V. Crystallizing membrane proteins using lipidic mesophases. *Nat. Protoc.* **4**, 706–731 (2009).
34. Liu, W., Ishchenko, A. & Cherezov, V. Preparation of microcrystals in lipidic cubic phase for serial femtosecond crystallography. *Nat. Protoc.* **9**, 2123–2134 (2014).
35. Ishchenko, A., Cherezov, V. & Liu, W. Preparation and delivery of protein microcrystals in lipidic cubic phase for serial femtosecond crystallography. *J. Vis. Exp.* **2016**, e54463 (2016).
36. Liu, W. & Cherezov, V. Crystallization of Membrane Proteins in Lipidic Mesophases. *J. Vis. Exp.* e2501, <https://doi.org/10.3791/2501> (2011).
37. Svensson, O., Malbet-Monaco, S., Popov, A., Nurizzo, D. & Bowler, M. W. Fully automatic characterization and data collection from crystals of biological macromolecules. *Acta Crystallogr. Sect. D Biol. Crystallogr.* **71**, 1757–1767 (2015).
38. Popov, A. N. & Bourenkov, G. P. Choice of data-collection parameters based on statistic modelling. *Acta Crystallogr. Sect. D Biol. Crystallogr.* **59**, 1145–1153 (2003).
39. Cherezov, V. *et al.* Rastering strategy for screening and centring of microcrystal samples of human membrane proteins with a sub-10 μm size X-ray synchrotron beam. *J. R. Soc. Interface* **6**, 587–597 (2009).
40. Weierstall, U. *et al.* Lipidic cubic phase injector facilitates membrane protein serial femtosecond crystallography. *Nat. Commun.* **5**, 3309 (2014).
41. Hart, P. *et al.* The CSPAD megapixel x-ray camera at LCLS. In *X-Ray Free-Electron Lasers: Beam Diagnostics, Beamline Instrumentation, and Applications.*, <https://doi.org/10.1117/12.930924> (2012).
42. Barty, A. *et al.* Cheetah: software for high-throughput reduction and analysis of serial femtosecond X-ray diffraction data. *J. Appl. Crystallogr.* **47**, 1118–1131 (2014).
43. Herrmann, S. *et al.* CSPAD-140k: A versatile detector for LCLS experiments. *Nucl. Instruments Methods Phys. Res. Sect. A Accel. Spectrometers, Detect. Assoc. Equip.* **718**, 550–553 (2013).
44. Marin, E. *et al.* CysLT1R receptor complex with Zafirlukast (P21 space group) structure (SFX@LCLS). *Coherent X-ray Imaging Data Bank*, <https://doi.org/10.11577/1660938> (2020).
45. Marin, E. *et al.* CysLT1R_6RZ4. *Zenodo* <https://doi.org/10.5281/zenodo.4032826> (2019).
46. Marin, E. *et al.* CysLT2R_6RZ6. *Zenodo* <https://doi.org/10.5281/zenodo.4032836> (2019).
47. Marin, E. *et al.* CysLT2R_6RZ7. *Zenodo* <https://doi.org/10.5281/zenodo.4032837> (2019).
48. Marin, E. *et al.* S. CysLT2R_6RZ8. *Zenodo* <https://doi.org/10.5281/zenodo.4032840> (2019).
49. Marin, E. *et al.* CysLT2R_6RZ9. *Zenodo* <https://doi.org/10.5281/zenodo.4032841> (2019).
50. Pandy-Szekeres, G. *et al.* GPCRdb in 2018: adding GPCR structure models and ligands. *Nucleic Acids Res.* **46**, D440–D446 (2018).
51. Marin, E. *et al.* CysLT1R receptor complex with Zafirlukast (P1 space group) structure (SFX@LCLS). *Coherent X-ray Imaging Data Bank* <https://doi.org/10.11577/1660939> (2020).

Acknowledgements

SWSX data analysis and treatment was supported by Russian Science Foundation (project no. 19-74-00088). XFEL sample preparation and SFX data analysis was done with support of grant 19-29-12022 from the Russian Foundation for Basic Research (RFBR). A.L., A.R., V.G., A.M. and V.B. are thankful for the Ministry of Science and Higher Education of the Russian Federation (agreement # 075-00337-20-03, project FSMG-2020-0003). V.P. acknowledges support by the project Structural Dynamics of Biomolecular Systems (ELIBIO) (CZ.02.1.01/0.0/0.0/15_003/0000447) from the European Regional Development Fund and the Ministry of Education, Youth and Sports (MEYS) of the Czech Republic. Use of the Linac Coherent Light Source (LCLS), SLAC National Accelerator Laboratory, is supported by the U.S. Department of Energy, Office of Science, Office of Basic Energy Sciences under Contract No. DE-AC02-76SF00515. We acknowledge the European Synchrotron Radiation Facility for provision of beam time on ID23-1, ID30a3, ID29 and ID30b and we would like to thank structural biology group for assistance. V.C. acknowledges that the University of Southern California is his primary affiliation.

Author contributions

E.M. performed SWSX data collection, processed SFX and SWSX data, organized raw data and wrote the manuscript. A.L. produced and crystallized protein, performed SWSX data collection and wrote the manuscript. A.G. produced and crystallized protein, performed SWSX data collection and wrote the manuscript. K.K. performed SWSX data collection and processed SWSX data. S.B. deposited the data and helped with manuscript preparation. P.K. produced protein. V.P. helped with crystal harvesting and SWSX data collection. E.L. produced protein. A.R. deposited the data. V.G. supervised the project. A.M. performed SWSX data collection, helped with manuscript preparation and supervised the project. V.C. performed SFX data collection, wrote the manuscript and supervised the project. V.B. performed SWSX data collection, wrote the manuscript and supervised the project.

Competing interests

The authors declare no competing interests.

Additional information

Supplementary information is available for this paper at <https://doi.org/10.1038/s41597-020-00729-2>.

Correspondence and requests for materials should be addressed to V.C. or V.B.

Reprints and permissions information is available at www.nature.com/reprints.

Publisher's note Springer Nature remains neutral with regard to jurisdictional claims in published maps and institutional affiliations.



Open Access This article is licensed under a Creative Commons Attribution 4.0 International License, which permits use, sharing, adaptation, distribution and reproduction in any medium or format, as long as you give appropriate credit to the original author(s) and the source, provide a link to the Creative Commons license, and indicate if changes were made. The images or other third party material in this article are included in the article's Creative Commons license, unless indicated otherwise in a credit line to the material. If material is not included in the article's Creative Commons license and your intended use is not permitted by statutory regulation or exceeds the permitted use, you will need to obtain permission directly from the copyright holder. To view a copy of this license, visit <http://creativecommons.org/licenses/by/4.0/>.

The Creative Commons Public Domain Dedication waiver <http://creativecommons.org/publicdomain/zero/1.0/> applies to the metadata files associated with this article.

© The Author(s) 2020, corrected publication 2020